Nature Communications

https://doi.org/10.1038/s41467-026-71042-6

Article in Press

Network model for alignment, stitching and slice-to-volume 3D reconstruction of large-scale spatially resolved slices

Received: 19 August 2025

Accepted: 12 March 2026

Cite this article as: Wang, Y., Liu, Z., Ma, X. Network model for alignment, stitching and slice-to-volume 3D reconstruction of large-scale spatially resolved slices. *Nat Commun* (2026). https://doi.org/10.1038/s41467-026-71042-6

Yu Wang, Zaiyi Liu & Xiaoke Ma

Network model for alignment, stitching and slice-to-volume 3D reconstruction of large-scale spatially resolved slices

Yu Wang[1, 2], Zaiyi Liu[3, 4], Xiaoke Ma[1, 2, 5*]

[1]School of Computer Science and Technology, Xidian University, No.2 South Taibai Road, Xi'an, 710071, Shaanxi, China.
[2]Key Laboratory of Smart Human-Computer Interaction and Wearable Technology of Shaanxi Province, Xidian University, No.2 South Taibai Road, Xi'an, 710071, Shaanxi, China.
[3]Department of Radiology, Guangdong Provincial People's Hospital (Guangdong Academy of Medical Sciences), Southern Medical University, 106 Zhongshan Er Road, Guangzhou, 510080, Guangzhou, China.
[4]Guangdong Provincial Key Laboratory of Artificial Intelligence in Medical Image Analysis and Application, Guangdong Provincial People's Hospital, Guangdong Academy of Medical Sciences, 106 Zhongshan Er Road, Guangzhou, 510080, Guangzhou, China.
[5]Shenzhen Loop Area Institute, No. 6 Hongmian Road, Fubao District, Shenzhen, 518017, Guangdong, China.

*Corresponding author(s). E-mail(s): xkma@xidian.edu.cn;

Abstract

Advances in spatially resolved technologies enable the characterization of tissues at molecular resolution by preserving spatial information. However, integrating and aligning spatial-omics data across different platforms and modalities remains challenging. Flexible tools for slice alignment, stitching and slice-to-volume 3D reconstruction are still lacking because available spatial-omics datasets are affected by partial overlapping, local non-rigid deformations, and large-scalability. Here we propose GEASO (Graph-based Elastic Alignment for Spatial-Omics data), a network-based algorithm for slice alignment, stitching and slice-to-volume 3D reconstruction. GEASO learns consistent spot features with graph neural network, and performs elastic registration to address rigid transformation

and local deformation of slices by exploiting topological structure of spot connectivity graphs. GEASO also adopts acceleration strategies to enable its application to large-scale datasets. Experiment results demonstrate that GEASO outperforms state-of-the-art baselines in alignment, stitching and 3D reconstruction of slices across various platforms, modalities and tissues, providing a versatile tool for analyzing spatial-omics data.

Introduction

Spatial-omic technologies [1], such as Visium [2], HDST [3], Xenium [4], Slide-seq [5], and Stereo-seq [6], effectively generate profiles of molecular characteristics within spatial context on intact tissue, providing unprecedented insights into organizations and functions of organs (e.g., breast [7], prostate [8], pancreas [9] and carcinoma [10]) and healthy tissues (e.g., human brain [11], heart [12], and mouse olfactory bulb [13]), as well as other applications [14, 15]. Therefore, it is of great significance for analyzing the accumulated spatially resolved omics data for uncovering complex mechanisms of biological systems. Although great efforts has been devoted to the analysis of two-dimensional spatial slices [16–21], attempts for three-dimensional (3D) reconstruction from serial spatial slices are really limited.

Actually, it is critically important to develop a slice-to-volume 3D reconstruction framework, since dynamics of molecular processes and cell-cell interactions usually occur within 3D circumstance [22, 23]. For example, *3D digital embryo* of mouses at single-cell resolution is achieved by aligning and stitching a series of spatial slices, revealing key signals governing the development of different important organs, such as heart and foregut [24]. However, it typically requires manually corrected spatial coordinates of all slices, requiring substantial manual labors. Consequently, many efforts are devoted to slice-to-volume 3D reconstruction by automatically aligning multiple slices. For instance, PASTE [25] adopts optimal transport to align pairwise slices, which is only suitable for highly similar slices. And, its variants PASTE2 [26] and Moscot [27] introduce partial-overlapping awareness alignment of slices from the same platforms. SLAT [28] addresses heterogeneity of slices across various platforms with graph-based adversarial matching [29], failing to address spatial transformation of slices. SANTO [30] learns spot features and performs alignment of slices via cross-slice correlation of spots within overlapping regions. However, it is criticized for ignoring local displacements of spots, resulting in biased 3D reconstructions. SPACEL [31] performs slice alignment by exploiting the manually annotated spatial domains within slice, and STAlign [32] transforms slice alignment problem into the conventional image registration task with manually selected landmarks. CAST [33] addresses deformation of slices with global alignment of pairwise slices, ignoring partially overlapped ones, and Spateo [34] simultaneously addresses partial overlapping and deformation of slices for 3D reconstruction. However, it is criticized for the unrealistical non-rigid transformation and failed to alignment slices with different spatial scale [35], which is difficult for aligning super-large scale slices and preserving the complex shapes of tissues.

Here, we simultaneously address alignment, stitching and slice-volume 3D reconstruction of large-scale spatially resolved slices with partial overlapping, rigid transformation, and local non-rigid deformation by proposing a flexible network-based framework, GEASO (Graph-based Elastic Alignment for Spatial-Omics data), which leverages the local topological structure of spot connectivity graphs of slices. The underlying assumption is that neighboring spots share similar transformation and deformation that provide clues for effective and efficient 3D reconstruction of objects [36–38]. As shown in Fig. 1, GEASO first constructs a spot connectivity graph for each slice, and employs graph neural network (GNN) to learn low-dimensional consistent features of spots by integrating spatial and expression profile of spots. GEASO then performs elastic registration to address partial overlapping, rigid transformation and local deformation of slices, where coarse alignment handles rigid transformation with Gaussian mixture model, and local non-rigid deformation is addressed with elastic registration by fully exploiting relations of topological structures of spots. Finally, GEASO addresses time complexity of large-scale slices with matrix low-rank approximation and down-sampling strategies, thereby dramatically extending applications of GEASO for large-scale datasets. Experimental results demonstrate that GEASO outperforms state-of-the-art methods in terms of accuracy for aligning, stitching and 3D reconstructing of spatial slices. And, it is also applicable for large-scale slices across various platforms, providing a comprehensive and useful approach for analyzing spatial-omics datasets. The superiority of GEASO over state-of-the-art baselines are summarized in Supplementary Table. 1.

Results

GEASO precisely addresses transformation and scalability of spatial slices with network model

Alignment of spatial slices is a fundamental problem for 3D reconstruction of tissues and organs, facing several critical challenges, such as heterogeneity of slices across various platforms, rigid transformation of slices, local deformation (non-rigid transformation) of slices, partial overlapping between slices, and large-scale of slices (Fig. 1**A**). Here, we simultaneously address all these challenges by proposing a flexible network-based model (called GEASO) for aligning, stitching and slice-to-volume 3D reconstructing of spatial slices, which consists of three typical modules, i.e., feature learning, elastic registration and acceleration strategies (Fig. 1**B**).

Specifically, the feature learning module considers the inconsistent expression profile and physical coordinates caused by different spatial platforms, individual variation and experimental batch effects. GEASO first constructs an attributed graph for each slice, converting alignment of slices into the alignment of attributed graphs, thereby avoiding heterogeneity of slices across various platforms. Then, GEASO employs graph neural network (GNN) with the constructed attributed graphs to extract consistent features of spots by fusing spatial coordinate and expression profiles of spots, where consistence and invariance of platforms are guaranteed with self-supervised learning strategy, facilitating downstream tasks such as registration and alignment of slices (see "Methods").

The elastic registration module addresses the rigid and non-rigid transformation of slices by exploiting the learned features and spot connectivity graphs, which is under the assumption that spots and their neighbors share similar graph local structure during slice deformation [37, 39]. In other words, GEASO leverages local topological consistency of spot connectivity graphs to align pairs of spots from source and target slices with similar features, topological structures, and expression profile under these circumstances. First, coarse alignment addresses rigid transformation of slices by estimating parameters for rotation, scale and translation with global information of slices. Then, partial overlapping between slices is addressed by a Gaussian mixture model, whose parameters are optimized by using expectation–maximization (EM) algorithm [40]. And, the registration module addresses non-linear local deformations of slices by incorporating a non-rigid displacement field for each spot, where global transformation and local deformation of slices are simultaneously modeled. Furthermore, spatial distance, expression profile, and topological structure of spots are integrated to estimate motion coherence, providing a more comprehensive and precise way to model transformation of slices. Finally, elastic registration is formulated as probabilistic model and optimized using Variational Bayesian inference [41] (see "Methods").

We also notice that nearly all current methods fail to address scalability of slices, which are critically needed since advances of biological technologies generate large-scale spatial slices. To overcome this limitation, GEASO also proposes the acceleration strategy to reduce time and space complexity, which preserves accuracy of slice alignment with two strategies, i.e., low-rank approximation of spot connectivity graphs, and interpolation of deformation with voxel-based down-sampling. In details, GEASO dramatically reduces complexity of large-scale spot connectivity graphs with low-rank approximation by preserving features of sampled spots, where global topological information is directly and approximately obtained from low-rank approximation. Furthermore, GEASO also employs the voxel-grid based down-sampling to reduce scale of slices, and infers rigid and non-rigid transformation with portion of these sampled spots by exploiting topological structure of graphs of spots (see "Methods").

Fig. 1**C** illustrates some typical applications of GEASO, i.e., alignment and stitching of slices, slice-to-volume 3D reconstruction, visualization of target organs, and topology analysis in 3D context, covering many critical fields of spatial genomics, providing a flexible and powerful tool for analyzing spatial-omics data.

Benchmarking GEASO on the alignment, stitching and 3D reconstruction of slices

To comprehensively evaluate the performance of GEASO, eight recent state-of-the-art methods, including PASTE [25], PASTE2 [26], SPACEL [31], STAlign [32], Moscot [27], SLAT [28], CAST [33] and Spateo [34], are selected as baselines on various datasets. And, four metrics, including PCC (Pearson correlation coefficient), CLC (contextual label consistency), AAS (alignment angle score), and MAE (mean absolute error), are chosen to fully validate performance of various algorithms under different conditions (see "Methods"). Specifically, PCC and CLC measure similarity in terms of expression profile level and cell type annotation between spatially proximal spots across two slices, whereas AAS quantifies difference between the predicted and truth

angles, and MAE evaluates the distance between predicted and ground-truth spatial coordinates, respectively.

We first validate performance of these algorithms on rigid transformation by simulating rotation angles of slices only. Specifically, two mouse brain slices sequenced by STARmap PLUS [42] are selected, and we fix one slice as target slice, and manually rotate another slice (i.e., source slice) with different angles from 30 to 180 (^{o}). Fig. 2**A** visualizes the original and alignment results of various algorithms on the simulated slices with angle as 90 and 135, where almost all these algorithms precisely recover the rotation angle, except for CAST since over-ration exists (dashed squares). Furthermore, GEASO not only precisely estimates angles of slice rotation, but also achieves the best performance under different metrics. In details, PCC of GEASO is 0.173, whereas those of others are less than 0.168. For example, CAST and Spateo over-transformed the CA regions in left bottom, resulting in unrealistic shapes (dashed squares), and Moscot can only performs rigid transformation, result in significant difference in top and bottom regions in source slice (top dashed squares of slices). The similar tendency repeatedly occurs by changing angles of rotation (bottom of Fig. 2**A** and Supplementary Fig. 1). Performance of these algorithms for rigid transformation in terms of PCC, CLC and AAS is shown in Fig. 2**B** and Supplementary Fig. 2, where GEASO is superior to all baselines. For instance, CLC of GEASO is 0.406±0.009, which is roughly two times that of PASTE (0.188±0.084), and roughly three times of SLAT (0.143±0.077) under all these cases, demonstrating that spot pairs aligned with GEASO are with higher similarity than those by others. We also investigate performance of various algorithms for no-rigid transformation of slices, where only CAST and Spateo, two methods that are capable of non-rigid transformation without prior knowledge are selected as baselines for fair comparison. GEASO also achieves the best PCC, outperforms CAST and Spateo (Supplementary Fig. 3**A** and **B**). These results further demonstrate that GEASO is promising for transformation of slices.

Then, we validate performance of various algorithms for stitching of two slices sequenced from mouse hippocampus region [43] with different overlapping ratio and rotation angles, where spots in source slice are colored in orange, and spots in target are colored in blue (Fig. 2**C** left panel). Since the ground truth spatial coordinates of spots are available, MAE is adopted as metric. Fig. 2**C** visualizes results of various algorithms for slice stitching, where GEASO always achieves the best performance. Specifically, Spateo, SPACEL, STAlign and GEASO precisely estimate angles of rotation and align overlapped regions of slices, whereas CAST and Moscot fail to address either of them with 30^o angle and 40% overlapping ratio. It is worth noting that SPACEL and STAlign require prior knowledge to stitch slices, which substantially influences their performance. For instance, performance of SPACEL for stitching slices decreases significantly as overlapping ratio decreases from 40% to 20%. Moreover, MAE of GEASO is significantly smaller than those of baselines for all these conditions, demonstrating that slices aligned by GEASO are much more close to the ground truth than baselines (Fig. 2**D**, Supplementary Fig. 4). Although MAEs of GEASO and Spateo are relative close (5.4 vs 14.8), the difference between alignment results obtained by these algorithms is also observable (Supplementary Fig. 5). In the challenging scenario involving both non-rigid deformation and partial overlapping

(Supplementary Fig. 3**C**), only GEASO and STAlign-GT (STAlign with landmarks) accurately stitch these slices, whereas CAST fails to address this issue as its reliance on global alignment prevents it from addressing local non-rigid transformations. And, Spateo also produce implausible displacements for non-rigid transformation. These results demonstrate that GEASO is precise and robust for stitching slices without requiring prior information.

We further benchmark all these algorithms on slice-to-volume 3D reconstruction with two datasets, i.e., mouse hemibrain MERFISH dataset with 129 slices and 9.3 million cells [44] (Fig. 2**E**) and human metastatic lymph node OpenST dataset with 19 slices and ∼1 million cells (Fig. 2**F**). All these algorithms perform slice-to-volume 3D reconstruction by setting the first slice as reference, and each slice is aligned to its previous one in sequence. Visualization of 3D reconstruction of mouse hemibrain tissue demonstrates that GEASO, STAlign and Spateo obtain smooth surfaces of organs, whereas Moscot and PASTE (PASTE2) fail because these algorithms cannot correctly estimate rotation angles of slices (Fig. 2**E**, Supplementary Fig. 6**A**). And, CAST distorts 3D structure of organs because it mistakenly estimates the scale factor, and it solely utilizes global information for non-rigid transformation, failing to address partial overlap and local deformation of slices. Since ground-truth coordinates of spots are available [45], GEASO achieves the best performance for 3D reconstruction of mouse brain with the minimal MAE (Fig. 2**E** right). The Human metastatic lymph node dataset [46] is further employed to evaluate the generalization of GEASO. As no ground-truth coordinates is available for this dataset, CLC is employed to evaluate performance of algorithms. The experimental results demonstrate that the surface of 3D architecture of organs reconstructed by GEASO is much smoother than those by baselines (Fig. 2**F** left, Supplementary Fig. 6**B**), demonstrating that the proposed algorithm can even precisely characterize heterogeneity of tumor tissues. There are two reasons to explain why GEASO is superior to baselines on the 3D reconstruction of organs. First, GEASO fully utilizes the local topological structure of spot graphs, which can precisely model heterogeneity of tumor tissues. Furthermore, GEASO also obtains the highest CLC score (0.410±0.067), followed by Spateo (0.303±0.054) that incorrectly aligns slice 8 and 9 (Fig. 2**F** right). Second, GEASO proposes two strategies to correct alignment errors, i.e., mesh-guided correction with known reference and mesh-free multi-slice refinement without reference (Supplementary Fig. 7). To investigate performance of these two correction strategies, we compare 3D architecture of organs reconstructed by various algorithms without and with correction, where GEASO consistently achieves the smallest accumulated misalignment errors, demonstrating effectiveness of GEASO for slice-to-volume 3D reconstruction of organs.

Finally, we also investigate the contribution of each component to GEASO with an ablation study (Supplementary Fig. 8**A**-**B**), demonstrating that all these components are necessary and critical for performance of GEASO, and the acceleration strategy contributes to speed of GEASO, respectively. We also explore the efficiency of GEASO in terms of runtime and memory usage by comparing it to all baselines, where GEASO is more computationally efficient and scalable to large-scale spatial omics data (Supplementary Fig. 8**C**-**F**). We also evaluate the robustness of GEASO against various

down-sampling rates (Supplementary Fig. 9) and noise levels (Supplementary Fig. 10), where GEASO is also insensitive to both down-sampling and noise.

GEASO bridges platforms of various resolutions and genome coverage with alignment and stitching of slices

Currently, many spatial platforms are available for spatially resolved data with various resolutions and coverage of genome. For example, Visium platform utilizes barcode-based technology to enhance coverage of genome by sacrificing resolutions, whereas Xenium is based on imaging-based techniques with single-cell resolution and low genome coverage. Thus, bridging platforms with various resolutions and genome coverage is promising for revealing mechanisms of biological systems. Here, we validate capability of GEASO for bridging various platforms with alignment and stitching of slices. The human breast cancer dataset [47] is deliberately selected since it consists of two slices from Xenium and one slice from Visium of same human breast cancer section, where slices of Visium contains 4,992 spots and 17,943 genes, and slices from Xenium are partially overlapped, where each contains about 100,000 cells and 313 genes (Fig. 3**A**). Cell-type annotations of these three slices are obtained by applying RCTD [18] to the corresponding scFFPE reference dataset (Fig. 3**B**).

Prior to bridging these two platforms, we first perform stitching among two slices generated by Xenium platform, as shown in Fig. 3**C**, where these slices are well stitched by GEASO since cell types are precisely aligned. However, almost all baselines fail to stitch cancer-related slices except for STAlign and SPACEL, which require prior knowledge to guide the alignment (Supplementary Fig. 11**A**), and the slice stitching performance obtained by different algorithms is measured in terms of PCC and CLC (Supplementary Fig. 11**B**). Then, to testify whether stitched slice provides deeper insights into breast cancer, we take the ductal carcinoma in situ (DCIS) region (black squares) as an illustrative example to demonstrate superiority of stitching. Specifically, DCIS in slice 1 of Xenium exhibits a hollow ring, whereas it corresponds to the center in slice 2 without ring structure (Fig. 3**D** top). Interestingly, structure of DCIS is restored after stitching, demonstrating that GEASO precisely aligns spots with the same cell types across various slices. Furthermore, we investigate possible reasons to account for improvement of stitching slices. Since GEASO fully utilizes topological structure of graphs of spots, and we compare topology of subnetwork corresponding to DCIS in various graphs. The bottom panels of Fig. 3**D** visualizes topological structure of DCIS in each graph, where DCIS corresponds to a cluster in each graph, and modularity structure is more obvious after stitching. Furthermore, we also quantify difference of spots inside and outside of DCIS in terms of degree and closeness centrality as shown in Fig. 3**E**. Surprisingly, the difference is significant between DCIS and surrounding regions, proving that stitching slices enhances completeness of the tissue architecture (two-sided Mann-Whitney U test for significance). Similar tendency also occurs in the lower-left DCIS region (Supplementary Fig. 12**A**). It is significant that GEASO accurately stitches the two Xenium slices, where slice 1 provides a more complete view of upper-right region of DCIS, and slice 2 better captures the low-left region of DCIS. By merging these complementary views, the stitched result achieves a more complete spatial delineation of the DCIS region. Furthermore, both the degree and

closeness centrality of spots in the stitched regions are significantly greater than in either individual slice (Supplementary Fig. 12**B**). These results convey two advantages of GEASO. First, structure of spots in spatial slices can be precisely reflected by topological structure of graphs, demonstrating that network models are promising for modeling spatially resolved data. Second, topological structure of graphs of spots provides additional information to facilitate alignment of cancer slices.

Moreover, Fig. 3**F** demonstrates that GEASO precisely identifies the overlapped regions by aligning slices across platforms and scales, whereas baselines fail to simultaneously address these two factors (Supplementary Fig. 13). For example, the well-known biomarker of breast cancer [48]*ABCC11* displays a consistent spatial expression pattern across both these two platforms (Fig. 3**G**), demonstrating that bridging various platforms facilitates the identification of critical cancer genes. Furthermore, we ask whether limitations of genome coverage of Xenium platform can be leveraged by Visium platform, and GEASO addresses this issue by imputing expression profile of genes in Xenium from those in Visium. Specifically, Poisson model implemented by scikit-leran package [49] is constructed with shared genes between Xenium and Visium slices, then predict expression level of missing genes in Xenium with those from spots within overlapping area in Visium (see: "Methods"). Fig. 3**H** visualizes spatial distribution of expression of two bio-marker genes, *ECM1* from invasive tumor [50] region and *SCGB2A2* from DCIS region [51], and spatial distribution of these predicted genes are higly consistent with the known cell type annotation, demonstrating the possibility and superiority of GEASO for bridging various platforms.

GEASO tracks evolution of organs with slice-to-volume 3D reconstruction

Previous experiments validate the performance of GEASO for aligning and stitching of pairwise slices, and it is natural to further investigate its capacity for multiple slices. Therefore, we select two whole-embryo cell atlases generated by Stereo-seq at embryonic day 9.5 (E9.5) and day 11.5 (E11.5) [6], where E9.5 atlas is with 90 slices and ∼900,000 cells (Fig. 4**A**), and E11.5 atlas with 84 slices and about 7,000,000 cells (Fig. 4**B**). And, all spots are manual annotated [52].

GEASO performs slice-to-volume 3D reconstruction of mouse embryo for E9.5 and E11.5 with pairwise elastic registration, and visualization of 3D architecture of embryo obtained by GEASO with three perspectives is shown in Fig. 4**A** and **B**. Spateo and OT-based methods (including Moscot, PASTE and PASTE2) are selected as baselines, as other methods cannot be applied to large-scale these datasets or require prior knowledge. By comparing 3D architecture of embryo obtained by GEASO and baselines (Fig. 4**C**), surface of embryo reconstructed by GEASO is significant smoother than those by baselines, and GEASO also significant superior to baselines in terms of CLC (Mann-Whitney U test for significance). These results demonstrate that GEASO precisely models transformation and deformation of slices that cannot be addressed with current baselines, thereby accurately reconstructing intricate 3D architecture of mouse embryo, which provides clues for biologists for down-stream analysis. Furthermore, we check spatial distribution of bio-marker genes for different organs to validate

correctness of 3D architecture reconstructed by GEASO. Fig. 4**D** visualizes 3D architecture of Heart and Liver at E9.5, where spatial distribution of the corresponding bio-marker gene *Myl7* and *Aft* is consistent with structure of organs, showing that elastic registration of GEASO accurately models intricate structure from slices. And, the same tendency repeats at E11.5, as shown in Fig. 4**E** and Supplementary Fig. 14**A**, showing that GEASO is robust for various datasets.

We subsequently segment the 3D architecture of brain from the reconstructed 3D embryo, as demonstrated in Fig. 5**A**, which can be further divided into four subdomains (Fig. 5**B**), providing a more comprehensive characterization of organs than 2D slices. We then leverage these 3D sub-structures to perform volumetric differential expression analysis to identify domain-specific differentially expressed genes (DEGs) (Fig. 5**C**), where the spatial patterns of these DEGs are highly expressed within its corresponding 3D domains, and substantially lowly expressed outside (Fig. 5**D**). The spatial specificity of these biomarker genes may provide insights into organ organization beyond known anatomical observations in the 2D context.

With the reconstructed 3D architecture of mouse embryo, evolution of organs can be effectively studied by investigating dynamics of developments of tissues. Fig. 4**F** shows that volume of Heart is much larger than Liver at E9.5, whereas volume of Heart and Liver is similar at E11.5. These results demonstrate that organs are developed at various stages with different speed, which possibly provides clues for biologists. Moreover, we also focus on dynamics of Heart and Liver by comparing expression of corresponding bio-marker genes at the micro-level, and Heart bio-marker gene *Myl7* and Liver bio-marker *Afp* are significantly differentially expressed between E9.5 and E11.5 (Supplementary Fig. 14**B**). Then, we also want to check whether dynamics of organs can also be reflected by topological structure of graphs of spots. Fig. 4**F** shows that degrees of spots within Heart is significantly higher than those in Liver at E9.5 (p¡2.2E-226, Mann-Whitney U test for significance), whereas this tendency completely reverses at E11.5 (Fig. 4**G**). These results further prove that dynamics of organs can be well characterized by topology of graphs, accounting for why GEASO outperforms baselines since it leverages performance of 3D reconstruction with graphs.

Currently, slices of organs are sequenced according to the fixed direction to fit size limitation of platforms, failing to provide comprehensive perspectives for organs. GEASO generates pseudo-slices along the arbitrarily pre-defined direction from the reconstructed 3D architecture of organs to facilitate downstream analysis (see "Methods", Fig. 4**H**). Specifically, these generated pseudo-slices provide clues for the consecutive tube-like neural tube (including brain and spinal cord), notochord, and gastrointestinal tract, etc. Furthermore, we also validate quality of pseudo-slices with the mouse brain dataset with 129 consecutive mouse coronal brain slices sequenced along the x-axis. Specifically, GEASO generates three pseudo-slices along the z-axis of the reconstructed 3D architecture of mouse brain (Supplementary Fig. 15**A**), which are highly consistent with the manually annotated mouse sagittal atlas from the Allen Brain Atlas [53] and the domains identified from real Visium slice using MNMST [54] (Supplementary Fig. 15**B**), and the proportions of spatial domains of pseudo-slices are consistent with those of real Visium slice (Supplementary Fig. 15**C**), demonstrating that pseudo-slices preserve critical spatial information of real ones. We further validate

whether the pseudo-slices facilitate downstream analysis, i.e., spatial domain identification and bio-marker gene discovery. Specifically, CAST is employed to identify spatial domains on these pseudo-slices, where the identified spatial domains are highly consistent with these manually annotated regions (Supplementary Fig. 16**A**). We then conduct differential expression analysis for spatial domains in pseudo slices (Supplementary Fig. 16**B**), and these identified DEGs are significantly highly expressed inside of their corresponding domains in all pseudo-slices, and lowly expressed outside (Supplementary Fig. 16**C**). These results suggest that these generated pseudo-slices are also applicable for identifying gene bio-markers, providing cues for downstream analysis.

Alignment and stitching of GEASO provide an effective way to integrate cross-modality slices

All these experiments carried on previous sections focus on slices with only a single modality generated by various platforms, i.e., implicitly existing strong relations among these slices. Here, we check whether GEASO is also capable of addressing cross-modality spatial slices because integrative analysis of spatial multi-omics data is the fundamental for revealing mechanisms of complex diseases. Two cross-modality slices sequenced from mouse brain for spatial transcriptomics and translatomes are selected, which are generated by STARmap [55] and RIBOmap [56] at single-cell resolution (Fig. 6**A**). Specifically, STARmap profiles RNA expression of genes, whereas RIBOmap selectively profiles the ribosome-bound RNA to probe protein translation in situ. And, both slices were annotated at cell type and region level.

Visualization of alignment of cross-modality mouse brain slices demonstrates that GEASO accurately aligns cell types of slices (Fig. 6**A**), where concordance rate of cell types across slices is 81.8 % (Supplementary Fig. 17), demonstrating that GEASO is also effective for aligning cross-modality spatial slices. Then, we investigate how alignment of cross-modality slices facilitates understanding translation efficiency. Specifically, single-cell relative translation efficiency (scRTE) [33], i.e., the normalized ratio of RIBOmap reads divided by STARmap reads for each spot, is selected to ensure the fair comparison of translation across cell types and regions. In *Oligodendrocytes*, the Myelin-associated genes *Mbp* and *Qdpr* are significantly up-regulated in terms of scRTE, whereas *Fth1* is down-regulated (Fig. 6**B** left), reflecting regional specificity of bio-markers for protein synthesis [57]. Similarly, in *Telencephalon Interneurons*, the translation elongation factor *Eef1a1* is significantly up-regulated, and *Kif5a* is down-regulated (Fig. 6**B** right). These results demonstrate that GEASO precisely aligns cross-modality slices, thereby providing clues for study translation efficiency of bio-marker genes in various regions.

Another additional cross-modality slices of juvenile mouse brain [58] for spatial transcriptomics and epigenomics sequenced by Spatial CUT & Tag-RNA-Seq slices are selected for a more comprehensive studies, where the spatial transcriptional slice is with 9,370 spots and 23,415 genes, and the the epigenetical slice with 9,548 spots for histone modifications *H3K4me3* (Fig. 6**C**). Actually, integrating spatial transcriptomics and eigenomics is promising since *H3K4me3* activates transcription of down-stream genes by regulating their enhancers. Visualization of alignment of slices is shown in Fig. 6**D**, where either slice cannot clearly boundaries of layers (dashed

squares). However, the aligned slice enhances boundary of layers, demonstrating that aligning transcriptional and eigenetical slices dramatically defines boundaries of layers. The possible reason is that transcription levels of spots on the boundary with differently activities of enhancers, thereby providing complementary information for transcriptions of genes. Furthermore, Fig. 6**E** visualizes R4 and R5 regions before and after alignment, where transcriptomics and epigenomics are much more consistent after alignment. We also quantify cell-type correspondence across two modality slices, and the heatmap plots demonstrate that slice alignment improves correlations among cell types (Fig. 6**F**).

Moreover, aligning slices across multi-modalities of these algorithms is benchmarked (Supplementary Fig. 18), where GEASO obtains the maximal CLC for domain R4, and is only slightly inferior to SPACEL. Notice that SPACEL explicitly exploits manually annotated spatial domains to guide slice alignment. These results further demonstrate that GEASO is promising for aligning slices across multi-modalities without prior information. And, the P22 mouse brain slices sequenced from *H3K27ac*, *H3K27me3*, and *ATAC* are selected to further validate performance of various algorithms (Supplementary Fig. 19**A**), where GEASO precisely aligns slices of *RNA* and *H3K27ac* because spatial distributions of domain **R4** and **R5** are highly consistent across slices (Supplementary Fig. 19**B**). The additional experiment for simultaneously aligning multiple slices (≥ 3) across different modalities is also executed (Supplementary Fig. 19**C**), where GEASO successfully aligns slices from *RNA*, *H3K27ac*, and *H3K4me3* within a common coordinate system. Domain R4 and R5 are highly consistent across all these three modalities, demonstrating that it can be naturally extended beyond pairwise alignment of slices. Finally, we check whether GEASO can generate pseudo multi-omics data by exploiting the aligned slices of multi-modalities. This process is achieved by aligning adjacent slices from distinct omics to identify anatomically overlapping regions, and subsequently stacking the multi-omic signals of spots within these shared regions. Specifically, by aligning slices of *RNA*, *H3K27ac* and *H3K4me3*, GEASO first identifies these spatial regions shared by all these slices (Supplementary Fig. 19**D**), consisting of 8,290 spots, and then corrects coordinates of spots for each slice according to the aligned slices. Visualization of the generated pseudo multi-omics data are presented in Supplementary Fig. 19**E**, where spots within domain **R4** and **R5** are highly consistent within the same coordinate system. These results further demonstrate that GEASO is versatile for various platforms and modalities.

Discussion

Alignment of spatial slices is a hot topic for analyzing spatially resolved data, and great efforts are devoted to it. However, many challenges remain because of complexity of spatial slices, such as slice heterogeneity, noise, rigid transformation, non-rigid deformation, and large dataset scale. In this study, we propose a flexible network-based algorithm for alignment of slices. In addition, we demonstrate that GEASO enables accurate alignment, stitching, and slice-to-volume 3D reconstruction of spatial slices across diverse platforms and modalities by jointly leveraging spatial coordinates, expression profiles, and topological information.

In summary, GEASO provides a versatile tool for analyzing spatial-omics data covering many typical circumstances. Specifically, GEASO is capable of aligning and stitching partially overlapping slices from different species and anatomical regions (Supplementary Fig. 20), thereby extending its potential applications, such as transferring annotation of slices (Supplementary Fig. 21). Thus, it not only can align similar slices as current algorithms, but also perform alignment with highly dissimilar ones, particularly these from different tissues or organs. Furthermore, such an multi-technology spatial slices integration algorithm will benefit users to fully utilize strengths of different spatial platforms for their studies, paving ways to reduce burdens of finance so that users adopt the combination of high- and low-resolution platforms. In other words, it is possible for biologists to fulfill their tasks with less budgets.

Furthermore, with well-reconstructed 3D architecture of organs obtained by GEASO, we can also generate pseudo-slices for organs and tissues at arbitrary directions, providing a more comprehensive perspectives to observe and characterize the original ones without additional labor costs. Moreover, we also demonstrate that GEASO seamlessly integrates spatial transcriptomics and epigenomics slices, investigating regulations of genes are studied with a more sophisticated strategy by combining protein-coding and non-coding elements of genome. With GEASO, biologists can also directly integrate slices of multiple modalities slices to reveal mechanisms and properties of systems from a comprehensive strategy.

We also see ample opportunity to enhance performance of GEASO. First, current version of GEASO only addresses spatially resolved data, and how to integrate additional image data, such as histology and morphology information, is very promising. In our previous studies [21], we demonstrate that morphological and transcriptional information of slices are complement. Second, GEASO solely focuses alignments of slices by solely learning and mapping conserved information across slices, ignoring specificity of slices that may also be interesting and critical for 3D reconstruction of tissues. Therefore, how to model and discriminate conserved and specific features of spots of cells are directions for future studies.

Methods

Ethics approval and consent to participate

No ethical approval was required for this study. All utilized public datasets were generated by other organizations that obtained ethical approval.

Problem definition

Let $\Psi = (X, Z)$ be a slice of n spots, where $X \in \mathbb{R}^{n\times 2}$ denotes coordinates of locations of spots, and $Z \in \mathbb{R}^{n\times n_Z}$ represents expression profiles of spots with n_Z genes/features. Let $\mathbf{x}_i$ be coordinates of the i-th spot. Given the source and target slice, denoted by $\Psi^{[s]} = (X^{[s]}, Z^{[s]})$ and $\Psi^{[t]} = (X^{[t]}, Z^{[t]})$, GEASO aims to align coordinates of spots

between $\Psi^{[s]}$ and $\Psi^{[t]}$ by constructing a transformation function $\mathcal{T}$ such that

$$\min_{\mathcal{T},P} \mathcal{L} = \sum_{i=1}^{n}\sum_{j=1}^{m} p_{ij}\|\mathbf{x}_i^{[t]} - \mathcal{T}(\mathbf{x}_j^{[s]})\|^2 \tag{1}$$

where $\mathcal{T}(\mathbf{x}_j^{[s]})$ is transformation function of spot $\mathbf{x}_j^{[s]}$, p_{ij} is the probability of alignment between $\mathbf{x}_j^{[s]}$ and $\mathbf{x}_i^{[t]}$, $\|X\|$ denotes Frobenius norm of matrix X, and n and m are the number of spots in target and source slice, respectively.

Since the source and target slices involve many unexpected deviations, such as rigid and non-rigid deformation, rotation and partial overlapping, it is highly non-trivial to accurately obtain transformation $\mathcal{T}$ and probability P for aligning and stitching spatial slices. GEASO addresses these issues with network-based models by exploiting topological structure of spot graphs for alignment and stitching with the assumption that neighboring spots share similar deformation [37, 39], which consists of three key components, including feature learning, elastic registration, and acceleration strategy.

Feature learning

If a pair of spots from the source and target slice are similar in terms of spatial proximity and transcription, p_{ij} is expected to receives heavy weight. To learn consistent features of spots from spatial and expression profile, we first construct an attributed graph of spots for each slice with K-nearest neighborhood (KNN), where edge weights correspond to reciprocal of Euclidean distance of spatial location between spots, and expression profiles are treated as attributes of spots (the number of neighbors of each spot is 8). And, we learn features of spots from these attributed graphs with graph neural network (GNN) [59]. Specifically, by treating expression profiles of spots as inputs of GNN, denoted by $H^{[0]}$, features of spots H for the $(l+1)$-th layer are obtained

$$H^{[l+1]} = \sigma(\alpha\widetilde{A}H^{[l]} + (1-\alpha)H^{[0]})(\beta I + (1-\beta)W^{[l]}) \tag{2}$$

where σ, $H^{[l]}$ and $W^{[l]}$ correspond to the activation function, features of spots, learnable linear projection of th l-th layer of GNN, $\widetilde{A}$ and I are the degree normalized adjacency matrix with self-loops of topological structure of graphs and identity matrix respectively, and parameter α and β control the relative importance of different items.

To address local deformation of slices, self-supervised learning module [60] is added by applying random masks onto vertices and edges of attributed graphs, which enhances robustness and discriminative of features. Specifically, two augmented slices $(A, \widehat{Z})$ and $(\widehat{A}, Z)$ are generated with mask operators. Given the corresponding features of spots $\widehat{H}_1$ and $\widehat{H}_2$, GEASO reduces impact of local deformation by minimizing the loss, i.e.,

$$\mathcal{L} = \|\widehat{H}_1 - \widehat{H}_2\|^2 + \lambda(\|\widehat{H}_1^{'}\widehat{H}_1 - I\|^2 + \|\widehat{H}_2^{'}\widehat{H}_2 - I\|^2) \tag{3}$$

where $H^{'}$ is the transpose of matrix H, and λ is a hyper-parameter. The training and optimization strategy for Eq.(3) are provided in the Supplementary Information.

Coarse alignment and stitching

As shown in Fig. 1, graph-based elastic registration of GEASO consists of two steps, i.e., coarse alignment with global information and refine alignment with local topology of graphs. Specifically, the rigid transformation of each spot $\mathbf{x}_i$ associated with rotation, scale and translation (Fig. 1**A** left panel) is formulated as

$$\mathcal{T}(\mathbf{x}_i; R, \boldsymbol{\upsilon}, s) = s\mathbf{x}_i R + \boldsymbol{\upsilon}, \tag{4}$$

where R, s and $\boldsymbol{\upsilon}$ correspond to the rotation matrix, scale parameter, and translation vector, respectively. By substituting Eq.(4) into Eq.(1), the coarse alignment of $\Psi^{[s]}$ and $\Psi^{[t]}$ is formulated as

$$\mathcal{L} = \sum_{i=1}^{n}\sum_{j=1}^{m} p_{ij}\|\mathbf{x}_i^{[t]} - s\mathbf{x}_j^{[s]}R - \boldsymbol{\upsilon}\|^2. \tag{5}$$

If the source and target slice are partially overlapped, stitching maps spots across slices with the Gaussian mixture model (GMM) by treating spots in source slice as centroid, and spots in target slice as data points. Specifically, the probability density function for each spot $\mathbf{x}_i^{[t]}$ is formulated as

$$f(\mathbf{x}_i^{[t]}) \propto \exp\{-\frac{1}{2\sigma^2}\|\mathbf{x}_i^{[t]} - \mathcal{T}(\mathbf{x}_j^{[s]}; R, \boldsymbol{\upsilon}, s)\|^2\} \tag{6}$$

where σ^2 is the variance. By substituting Eq.(6) into Eq.(5), the model of stitching slices is formulated as a likelihood function, i.e.,

$$\begin{aligned} &\frac{1}{2\sigma^2}\sum_{i=1}^{n}\sum_{j=1}^{m} p_{ij}\|\mathbf{x}_i^{[t]} - \mathbf{T}(\mathbf{x}_j^{[s]}; R, \boldsymbol{\upsilon}, s)\|^2 + N_p \log\sigma^2, \\ &s.t.\quad R^{'}R = I, det(R) = 1, \end{aligned} \tag{7}$$

where $N_p = \sum_{i=1}^{n}\sum_{j=1}^{m} p_{ij}$. And, Eq.(7) can be effectively solved with expectation maximization (EM) algorithm [40] (Supplementary Information).

Elastic Registration

Except for rigid transformation of slices, GEASO also addresses non-rigid transformation generated by deformations with the elastic registration $\mathcal{T}$, which incorporates the non-rigid displacement field $\Delta\mathbf{x}_j^{[s]}$ into each spot $\mathbf{x}_j^{[s]}$. Therefore, model for elastic registration is formulated as

$$\mathcal{L} = \sum_{i=1}^{n}\sum_{j=1}^{m} p_{ij}\|\mathbf{x}_i^{[t]} - s(\mathbf{x}_j^{[s]} + \Delta\mathbf{x}_j^{[s]})R - \boldsymbol{\upsilon}\|^2. \tag{8}$$

By following Ref. [61], we also hypothesize that displace field $\Delta\mathbf{x}^{[s]}$ is with motion-coherence prior that encourages neighbors of spots are with similar deformations, which also is one of major motivations of GEASO for 3D reconstruction in this study. In details, the conditional probability $p(\Delta\mathbf{X}|X)$ is defined as

$$p(\Delta\mathbf{x}|X) = \mathcal{N}(0, \lambda_{\Delta}^{-1} G \otimes I) \tag{9}$$

where $\otimes$ is the Kronecker product and $G \in \mathbb{R}^{m\times m}$ is the motion coherence matrix, and $\lambda_{\Delta} > 0$ is a positive parameter. To fully characterize motion coherence of spots, we incorporate spatial and topological information into the motion coherence matrix G with is a linear function as

$$G = (G^{(gst)} + \tau G^{(euc)})Q \tag{10}$$

where $\tau \in (0, 1)$ is a trade-off parameter, Q, $G^{(gst)}$ and $G^{(euc)}$ are similarity of spots in terms of features, the shortest path proximity and spatial proximity of spots, respectively. In this case, Eq.(10) fuses the topological, spatial location and features of spots, providing a more comprehensive way to model the local structure of slices.

Eq. (8) can be explicitly solved with Bayesian approaches. Specifically, let $\mathbf{c} = (c_1, \cdots, c_n) \in \{0, 1\}$ be the indicator vector, where c_i=0 if the i-th spot in target slice is an outlier, 1 otherwise. And, $\mathbf{e} = (e_1, \ldots, e_n) \in \{1, \ldots, m\}$ is index vector of spots to indicate which spot in target slice is generated from source slice. Therefore, probability of elastic registration between $\Psi^{[s]}$ and $\Psi^{[t]}$ is formulated as

$$\begin{aligned} &p(\Psi_i^{[t]}, c_i, e_i|\Psi^{[s]}, \Delta X, s, R, \boldsymbol{\upsilon}, \eta, \omega, \sigma^2) \\ &= \left(\omega p_o(\mathbf{x}_i^{[t]})\right)^{1-c_i} \left\{(1-\omega)\prod_{j=1}^{m}(\eta_j \phi(\mathbf{x}_i^{[t]}; \mathcal{T}(\mathbf{x}_j^{[s]}), \sigma^2 I) p_h(h_i^{[t]}|h_j^{[s]}))^{\delta_j(e_i)}\right\}^{c_i} \end{aligned} \tag{11}$$

where $p_o(\mathbf{x}_i^{[t]})$ is the probability of spot $\mathbf{x}_i^{[t]}$ being an outlier, $\phi(\mathbf{x}_i^{[t]}; \mathcal{T}(\mathbf{x}_j^{[s]}), \sigma^2 I)$ is the Gaussian density with mean $\mathcal{T}(x_j^{[s]})$ and variance σ^2, and $\eta = (\eta_1, \ldots, \eta_m) \in [0, 1]$ is probability for each spot in target slice, i.e., $\sum_{j=1}^{m} \eta_j = 1$. By modeling η with the Dirichlet distribution, the probability of elastic registration is formulated as

$$p(\Psi^{[t]}, \Psi^{[s]}) \propto p(\Delta X^{[s]}|\Psi^{[s]}) p(\eta) \prod_{i=1}^{n} p(\Psi_i^{[t]}, c_i, e_i|\Psi^{[s]}, \Delta X, \eta, s, R, \boldsymbol{\upsilon}, \sigma^2). \tag{12}$$

Eq.(12) is approximately solved with variation Bayesian inference (VBI) [41], and details are provided in supplementary Information.

Acceleration strategies for super-large scale slices

Super-large slices (i.e., number of spots is over 100,000) pose a great challenge on designing efficient algorithms for alignment, stitching and 3D reconstruction. Here, we

propose two strategies to accelerate GEASO (Fig. 1**B**). Specifically, there are two time-consuming components, i.e., the construction of motion coherence matrix G for source slice, and elastic registration. On the first concerning, we adopt Nyström method [62] to approximate graph G with three low-rank matrices, where approximation is guaranteed by spots sampled from the source slice (Supplementary Information).

On the elastic registration concerning, we address its complexity with down-sampling. Specifically, down-sampling is performed for both the source and target slice with voxel-grid filter [36] to alleviate errors of sampling, then alignment and stitching are performed on the sampled slices with parameters of rigid transformation $\hat{\mathcal{T}} = (\hat{s}, \hat{R}, \hat{\boldsymbol{\upsilon}})$ and deformation vectors $\Delta\hat{X}$. According to local structure constraint theory [39], we estimate deformation parameters of unsampled spots by exploiting their neighbors as

$$\begin{cases} \min_{\Delta\hat{X}^{[s]}} \mathcal{L}(\Delta\hat{X}^{[s]}, \hat{\mathcal{T}}, \hat{\Psi}^{[t]}, \hat{\Psi}^{[s]}) \\ \min_{\Delta X^{[s]}=\varphi(\Delta\hat{X}^{[s]})} \mathcal{L}(\Delta X^{[s]}, \hat{\mathcal{T}}, \hat{\Psi}^{[t]}, \hat{\Psi}^{[s]}) \end{cases} \tag{13}$$

where $\hat{\Psi}^{[s]}$ and $\hat{\Psi}^{[t]}$ are down-sampled slices, and φ is a Gaussian regression function [36] for restoring whole slice $\Delta X^{[s]}$ with sampled spots with interpolations. The detailed optimization procedures of Eq.(13) are provided in Supplementary Information.

Baselines and metrics for performance

Eight state-of-the-art methods, Spateo (v1.1.0) [63], Moscot (v0.4.3) [27], CAST (latest commit 3ebcf4f) [33], SLAT (v0.2.2) [28], STAlign (v1.0.0) [32], SPACEL (v1.1.8) [31], PASTE2 (latest commit 8d34bb4) [26] and PASTE (v1.4.0) [25] are selected as baselines because of popularity and excellent performance of these algorithms. The detailed hyperparameter settings for each algorithm are summarized in the Supplementary Information.

By following Refs. [30, 64], PCC (Pearson correlation coefficient), CLC (contextual label consistency score) and AAS (alignment angle score) are selected to evaluate performance of algorithms for slice alignment, and MAE (mean absolute error) is selected to evaluate performance of algorithms for slice stitching and 3D reconstruction when ground truth coordinates of spots are available. Specifically, given the source $\Psi^{[s]}$ and target $\Psi^{[t]}$ slice, PCC quantifies similarity of aligned spot pairs in terms of expression, i.e.,

$$PCC = \frac{1}{n}\sum_{i=1}^{n} PCC(\mathbf{z}_i^{[t]}, \mathbf{z}_{j^*}^{[s]}), \tag{14}$$

where $j^* = \arg\max_j p_{ij}$ and $\mathbf{z}_i$ is expression profile of the i-th spot in the corresponding slices.

On the rigid transformation issue, AAS measures difference of angles between the predicted and ground truth rotation, i.e.,

$$AAS = 2\pi - |R_{pred} - R_{gt}|, \tag{15}$$

where R_{pred} and R_{gt} is the predicted and ground truth rotation matrix, respectively. And, a higher AAS typically means a better alignment or stitching.

For slices whose spots are with ground truth coordinates, MAE evaluate spatial distances of aligned spot pairs, i.e.,

$$MAE = \frac{1}{m}\sum_{i=1}^{m}|\mathbf{x}_i{}^* - \mathcal{T}(\mathbf{x}_i)|, \tag{16}$$

where $\mathbf{x}_i{}^*$ is the ground-truth spatial coordinate of spot i, and $\mathcal{T}(x_i)$ is the transformed spatial coordinate. Typically, lower MAE means better transformation.

For slices without ground truth coordinates of spots, CLC measures the label consistency between spot i and its corresponding neighborhood in the other slice as

$$CLC(M) = \frac{1}{n}\sum_{i=1}^{n}\Big(\frac{1}{|\mathcal{N}_{j^*}|}\sum_{\mathbf{x}_k^{[s]}\in\mathcal{N}_{j^*}}\zeta(\vartheta(\mathbf{x}_k^{[s]}) = \vartheta(\mathbf{x}_i^{[t]}))\Big), \tag{17}$$

where $j^* = \arg\max_j p_{ij}$ and $\mathcal{N}_{j^*}$ is the neighbors of spots $\mathbf{x}_i^{[t]}$, $\vartheta(\mathbf{x}_i)$ is the label of spot $\mathbf{x}_i$, and $\zeta(a, b)$ is a function, 1 if $a = b$, 0 otherwise, respectively. CLC is degenerated to concordance rate if $\mathcal{N}_{j^*} = \{\mathbf{x}_{j^*}\}$, i.e., no neighbors is allowed.

Generation of pseudo slices

Given the 3D architecture of organs reconstructed by GEASO, we can thus generate pseudo slices along the custom pre-defined direction. Specifically, we first define the desired thickness of pseudo slices, denoted as Δd, which usually match the thickness of the original one. Then, we compute the axis length along the pre-defined direction (i.e., $z_{\max} - z_{\min}$) and determine the number of pseudo slices N_{slices}, i.e., $N_{\text{slices}} = \lceil (d_{\max} - d_{\min})/\Delta d \rceil$. All these spots whose coordinates falling in the same Δd interval are assigned to the corresponding pseudo slice. In such approach, spatial resolutions of pseudo slices are identical to those of the original ones, which successfully avoids introducing artifacts because of artificial interpolations.

Identification and functional analysis of differentially expressed genes

We perform differential expression analysis of genes for each spatial domain by using Wilcoxon rank-sum test implemented in SCANPY package [65]. Genes expressed in more than 80% of cells/spots in each domain, with a fold change $\geq$ 1.5 and an adjusted FDR $\leq$ 0.05, are selected as differentially expressed genes (DEGs). The filtered DEGs serve as input for gene ontology enrichment analysis, which is conducted with clusterProfiler [66]. Enriched functional terms with -log10(adjusted P-value) are plotted.

Data pre-processing

Ten datasets are selected to evaluate the performance of GEASO on three tasks, including slice alignment, slice stitching, and slice-to-volume 3D reconstruction. Specifically, the mouse hippocampus and brain slices sequenced using STARmap [42, 43], and the human dorsolateral prefrontal cortex (DLPFC) slices sequenced using 10× Visium [11] serve as benchmark for slice alignment and stitching. The mouse brain slices sequenced using MERFISH [44], human lymph node slices sequenced using OpenST [46], and mouse embryo slices sequenced using Stereo-seq [52] are employed for the slice-to-volume reconstruction task. Furthermore, the human breast cancer slices co-assayed with Visium and Xenium are selected to evaluate performance of algorithms on aligning and stitching slices across different spatial platforms with different resolutions. The spatial multi-modality datasets, such as the mouse brain slices co-assayed with STARmap (RNA) and RIBOmap (protein), and P22 juvenile mouse brain slices co-assayed with Spatial CUT & Tag and RNA-seq, are selected for experiments. The detailed description of all these datasets is provided in Supplementary Information.

For these datasets generated by spatially resolved transcriptomics technologies (including STARmap, Visium, Xenium, and MERFISH), genes expressed in less than 10 spots are removed for each slice, and the remained genes which shared across slices are kept for downstream analysis. The expression profile further normalized by library size and log-transformed using SCANPY [65]. For these mouse brain slices co-assayed using STARmap (RNA) and RIBOmap (protein), expression profiles of STARmap are filtered, normalized, log-transformed, and scaled without zero-centering, followed by principal component analysis (PCA) for dimension reduction (the number of dimensions is 50). Protein profiles of RIBOmap are normalized with centered log-ratio (CLR), and undertook dimension reduction with PCA (the number of dimensions is 50). For the P22 juvenile mouse brain slices, expression profiles are processed as that of STARmap. For the chromatin accessibility data (i.e., *H3K4me3*), peaks detected in less than 6% of spots are removed, then the top 3,000 highly variable peaks are selected, and the dimensionality further reduced to 20 using latent semantic indexing (LSI). These obtained features (embedding) serve as attributes of graphs.

We employ KNN to construct backbone (topological structure, i.e., spot connectivity graph) of attributed graphs for slices by varying values of parameter η, which control the number of neighbors for each spot in slices. Specifically, according to Squidpy [67], for slices sequenced using Visium whose spots are arranged in a regular hexagonal lattice, we set $\eta = 6$. For slices sequenced using MERFISH, STARmap, RIBOmap, and Stereo-seq, whose spots follow a grid-like arrangement, we set $\eta = 8$. For slices sequenced by Spatial CUT & Tag-RNA-Seq, these two slices share the same spatial resolution, and spots exhibit a grid-like arrangement, we therefore set $\eta = 8$ for both slices. And, for slices co-assayed using different spatial platforms with different spatial resolutions, such as the human breast cancer slices co-assayed using Visium (barcode-based, 55μm diameter per spot) and Xenium (imaging-based, single-cell spatial resolution), we set $\eta = 6$ for Visium slice, and $\eta = 20$ for the Xenium slice according to SLAT [28], ensuring that the spatial neighborhoods in both slices

cover similar areas, promoting consistent cell embeddings across datasets with different spatial resolutions. The analysis and settings of hyper-parameters of GEASO are also conducted (Supplementary Fig. 22, and Supplementary Table. 2).

Statistics and reproducibility

Statistical analyses were performed using standard computational packages (Python SciPy). Where applicable, statistical significance was evaluated using the two-sided Mann-Whitney U test, with exact P values and specific n numbers (representing biologically independent samples or individual cells) detailed in the respective figure legends.

No statistical method was used to predetermine sample size. No data were excluded from the analyses. The experiments were not randomized. The Investigators were not blinded to allocation during experiments and outcome assessment.

Data Availability

All datasets analyzed in this paper are published datasets and available for public download. The human dorsolateral prefrontal cortex data [11] used in this study are available in the spatialLIBD database (http://spatial.libd.org/spatialLIBD). The mouse brain (8 months) data [42] and mouse hippocampus data [43] used in this study are available in the Single Cell Portal database under accession codes SCP1375 (https://singlecell.broadinstitute.org/single_cell/study/SCP1375) and SCP1830 (https://singlecell.broadinstitute.org/single_cell/study/SCP1830). The serial mouse brain data [44] used in this study are available in the Brain Image Library database (https://doi.brainimagelibrary.org/doi/10.35077/act-bag). The human metastatic lymph node data [46] and mouse brain (Spatial CUT&Tag–RNA-seq) data [58] used in this study are available in the GEO database under accession codes GSE251926 (https://www.ncbi.nlm.nih.gov/geo/query/acc.cgi?acc=GSE251926) and GSE165217 (https://www.ncbi.nlm.nih.gov/geo/query/acc.cgi?acc=GSE165217). The human breast cancer data [4] used in this study are available in the 10× Genomics datasets database (https://www.10xgenomics.com/resources/datasets). The whole mouse embryo data [52] used in this study are available in the Spateo database (http://spateodata.aristoteleo.com). The spatial multi-omics mouse brain data [56] used in this study are available in the Single Cell Portal database under accession code SCP1835 (https://singlecell.broadinstitute.org/single_cell/study/SCP1835). The processed data generated in this study have been deposited in the Zenodo database (https://doi.org/10.5281/zenodo.18811760). Source data are provided with this paper.

Code Availability

The code for GEASO algorithm is implemented in Python and detailed tutorials are freely available at https://github.com/xkmaxidian/GEASO [68]. The source code of GEASO is released under the MIT License.

References

[1] Marx V. Method of the Year: spatially resolved transcriptomics. Nat Methods. 2021;18(1):9–14.

[2] Ståhl PL, Salmén F, Vickovic S, Lundmark A, Navarro JF, Magnusson J, et al. Visualization and analysis of gene expression in tissue sections by spatial transcriptomics. Science. 2016;353:78–82.

[3] Vickovic S, Eraslan G, Salmén F, Klughammer J, Stenbeck L, Schapiro D, et al. High-definition spatial transcriptomics for in situ tissue profiling. Nat Methods. 2019;16:987–990.

[4] Marco Salas S, Kuemmerle LB, Mattsson-Langseth C, Tismeyer S, Avenel C, Hu T, et al. Optimizing Xenium In Situ data utility by quality assessment and best-practice analysis workflows. Nature Methods. 2025;p. 1–11.

[5] Stickels RR, Murray E, Kumar P, Li J, Marshall JL, Di Bella DJ, et al. Highly sensitive spatial transcriptomics at near-cellular resolution with Slide-seqV2. Nat Biotechnol. 2021;39:313–319.

[6] Wei X, Fu S, Li H, Liu Y, Wang S, Feng W, et al. Single-cell Stereo-seq reveals induced progenitor cells involved in axolotl brain regeneration. Science. 2022;377:eabp9444.

[7] Andersson A, Larsson L, Stenbeck L, Salmén F, Ehinger A, Wu SZ, et al. Spatial deconvolution of HER2-positive breast cancer delineates tumor-associated cell type interactions. Nat Commun. 2021;12(1):6012.

[8] Berglund E, Maaskola J, Schultz N, Friedrich S, Marklund M, Bergenstråhle J, et al. Spatial maps of prostate cancer transcriptomes reveal an unexplored landscape of heterogeneity. Nat Commun. 2018;9(1):2419.

[9] Moncada R, Barkley D, Wagner F, Chiodin M, Devlin JC, Baron M, et al. Integrating microarray-based spatial transcriptomics and single-cell RNA-seq reveals tissue architecture in pancreatic ductal adenocarcinomas. Nat Biotechnol. 2020;38(3):333–342.

[10] Moncada R, Barkley D, Wagner F, Chiodin M, Devlin JC, Baron M, et al. Integrating microarray-based spatial transcriptomics and single-cell RNA-seq reveals tissue architecture in pancreatic ductal adenocarcinomas. Nature biotechnology. 2020;38(3):333–342.

[11] Maynard KR, Collado-Torres L, Weber LM, Uytingco C, Barry BK, Williams SR, et al. Transcriptome-scale spatial gene expression in the human dorsolateral prefrontal cortex. Nat Neurosci. 2021;24:425–436.

[12] Farah EN, Hu RK, Kern C, Zhang Q, Lu TY, Ma Q, et al. Spatially organized cellular communities form the developing human heart. Nature. 2024;627(8005):854–864.

[13] Maniatis S, Äijö T, Vickovic S, Braine C, Kang K, Mollbrink A, et al. Spatiotemporal dynamics of molecular pathology in amyotrophic lateral sclerosis. Science. 2019;364(6435):89–93.

[14] Cable DM, Murray E, Shanmugam V, Zhang S, Zou LS, Diao M, et al. Cell type-specific inference of differential expression in spatial transcriptomics. Nat Methods. 2022;19(9):1076–1087.

[15] Wu L, Yan J, Bai Y, Chen F, Zou X, Xu J, et al. An invasive zone in human liver cancer identified by Stereo-seq promotes hepatocyte–tumor cell crosstalk, local immunosuppression and tumor progression. Cell Res. 2023;p. 1–19.

[16] Hu J, Li X, Coleman K, Schroeder A, Ma N, Irwin DJ, et al. SpaGCN: Integrating gene expression, spatial location and histology to identify spatial domains and spatially variable genes by graph convolutional network. Nat Methods. 2021;18:1342–1351.

[17] Zhao E, Stone MR, Ren X, Guenthoer J, Smythe KS, Pulliam T, et al. Spatial transcriptomics at subspot resolution with BayesSpace. Nat Biotechnol. 2021;39:1375–1384.

[18] Cable DM, Murray E, Zou LS, Goeva A, Macosko EZ, Chen F, et al. Robust decomposition of cell type mixtures in spatial transcriptomics. Nat Biotechnol. 2022;40(4):517–526.

[19] Li J, Chen S, Pan X, Yuan Y, Shen HB. Cell clustering for spatial transcriptomics data with graph neural networks. Nat Comput Sci. 2022;2:399–408.

[20] Dong K, Zhang S. Deciphering spatial domains from spatially resolved transcriptomics with an adaptive graph attention auto-encoder. Nat Commun. 2022;13:1–12.

[21] Wang Y, Liu Z, Ma X. MuCST: restoring and integrating heterogeneous morphology images and spatial transcriptomics data with contrastive learning. Genome Med. 2025;17(1):21.

[22] Ueda HR, Ertürk A, Chung K, Gradinaru V, Chédotal A, Tomancak P, et al. Tissue clearing and its applications in neuroscience. Nature Reviews Neuroscience. 2020;21(2):61–79.

[23] Richardson DS, Lichtman JW. Clarifying tissue clearing. Cell. 2015;162(2):246–257.

[24] Xie P, Shen J, Yang Y, Wang X, Liu W, Cao H, et al. Digital reconstruction of full embryos during early mouse organogenesis. Cell. 2025;.

[25] Zeira R, Land M, Strzalkowski A, Raphael BJ. Alignment and integration of spatial transcriptomics data. Nat Methods. 2022;19(5):567–575.

[26] Liu X, Zeira R, Raphael BJ. Partial alignment of multislice spatially resolved transcriptomics data. Genome Res. 2023;33(7):1124–1132.

[27] Klein D, Palla G, Lange M, Klein M, Piran Z, Gander M, et al. Mapping cells through time and space with moscot. Nature. 2025;p. 1–11.

[28] Xia CR, Cao ZJ, Tu XM, Gao G. Spatial-linked alignment tool (SLAT) for aligning heterogenous slices. Nat Commun. 2023;14(1):7236.

[29] Gao J, Huang X, Li J. Unsupervised graph alignment with wasserstein distance discriminator. In: Proceedings of the 27th ACM SIGKDD Conference on Knowledge Discovery & Data Mining; 2021. p. 426–435.

[30] Li H, Lin Y, He W, Han W, Xu X, Xu C, et al. SANTO: a coarse-to-fine alignment and stitching method for spatial omics. Nature Communications. 2024;15(1):6048.

[31] Xu H, Wang S, Fang M, Luo S, Chen C, Wan S, et al. SPACEL: deep learning-based characterization of spatial transcriptome architectures. Nature Communications. 2023;14(1):7603.

[32] Clifton K, Anant M, Aihara G, Atta L, Aimiuwu OK, Kebschull JM, et al. STalign: Alignment of spatial transcriptomics data using diffeomorphic metric mapping. Nat Commun. 2023;14(1):8123.

[33] Tang Z, Luo S, Zeng H, Huang J, Sui X, Wu M, et al. Search and match across spatial omics samples at single-cell resolution. Nature methods. 2024;p. 1–12.

[34] Qiu X, Zhu DY, Lu Y, Yao J, Jing Z, Min KH, et al. Spatiotemporal modeling of molecular holograms. Cell. 2024;187(26):7351–7373.

[35] Tajdari F, Huysmans T, Yang Y, Song Y. Feature preserving non-rigid iterative weighted closest point and semi-curvature registration. IEEE Transactions on Image Processing. 2022;31:1841–1856.

[36] Hirose O. Acceleration of non-rigid point set registration with downsampling and Gaussian process regression. IEEE Transactions on Pattern Analysis and Machine Intelligence. 2020;43(8):2858–2865.

[37] Wang L, Chen R, Sun F, Wang X, Sun K, Zhong C, et al. Equivariant Local Reference Frames With Optimization for Robust Non-Rigid Point Cloud Correspondence. IEEE Transactions on Image Processing. 2025;.

[38] Liu M, Li G, Yu H, Song R, Li Y, Meng MQH, et al. LCNet: A Robust and Accurate Non-Rigid 3D Point Set Registration Approach for Image-Guided Liver Surgery. IEEE Transactions on Medical Robotics and Bionics. 2025;.

[39] Yuille AL, Grzywacz NM. A mathematical analysis of the motion coherence theory. International Journal of Computer Vision. 1989;3(2):155–175.

[40] Dempster AP, Laird NM, Rubin DB. Maximum likelihood from incomplete data via the EM algorithm. Journal of the royal statistical society: series B (methodological). 1977;39(1):1–22.

[41] Tzikas DG, Likas AC, Galatsanos NP. The variational approximation for Bayesian inference. IEEE Signal Processing Magazine. 2008;25(6):131–146.

[42] Zeng H, Huang J, Zhou H, Meilandt WJ, Dejanovic B, Zhou Y, et al. Integrative in situ mapping of single-cell transcriptional states and tissue histopathology in a mouse model of Alzheimer's disease. Nature Neuroscience. 2023;26(3):430–446.

[43] Shi H, He Y, Zhou Y, Huang J, Maher K, Wang B, et al. Spatial atlas of the mouse central nervous system at molecular resolution. Nature. 2023;622(7983):552–561.

[44] Zhang M, Pan X, Jung W, Halpern AR, Eichhorn SW, Lei Z, et al. Molecularly defined and spatially resolved cell atlas of the whole mouse brain. Nature. 2023;624(7991):343–354.

[45] Wang Q, Ding SL, Li Y, Royall J, Feng D, Lesnar P, et al. The Allen mouse brain common coordinate framework: a 3D reference atlas. Cell. 2020;181(4):936–953.

[46] Schott M, León-Periñán D, Splendiani E, Strenger L, Licha JR, Pentimalli TM, et al. Open-ST: High-resolution spatial transcriptomics in 3D. Cell. 2024;187(15):3953–3972.

[47] Janesick A, Shelansky R, Gottscho AD, Wagner F, Williams SR, Rouault M, et al. High resolution mapping of the tumor microenvironment using integrated single-cell, spatial and in situ analysis. Nat Commun. 2023;14(1):8353.

[48] Yoshiura Ki, Kinoshita A, Ishida T, Ninokata A, Ishikawa T, Kaname T, et al. A SNP in the ABCC11 gene is the determinant of human earwax type. Nature genetics. 2006;38(3):324–330.

[49] Pedregosa F, Varoquaux G, Gramfort A, Michel V, Thirion B, Grisel O, et al. Scikit-learn: Machine learning in Python. J Mach Learn Res. 2011;12:2825–2830.

[50] Wang L, Yu J, Ni J, Xu XM, Wang J, Ning H, et al. Extracellular matrix protein 1 (ECM1) is over-expressed in malignant epithelial tumors. Cancer letters. 2003;200(1):57–67.

[51] Rebbeck CA, Xian J, Bornelöv S, Geradts J, Hobeika A, Geiger H, et al. Gene expression signatures of individual ductal carcinoma in situ lesions identify processes and biomarkers associated with progression towards invasive ductal carcinoma. Nature communications. 2022;13(1):3399.

[52] Cheng M, Zheng H, Fang Q, Bai Y, Liu C, Pan H, et al. Three-dimension transcriptomics maps of whole mouse embryo during organogenesis. bioRxiv. 2024;p. 2024–08.

[53] Sunkin SM, Ng L, Lau C, Dolbeare T, Gilbert TL, Thompson CL, et al. Allen Brain Atlas: an integrated spatio-temporal portal for exploring the central nervous system. Nucleic Acids Res. 2012;41:D996–D1008.

[54] Wang Y, Liu Z, Ma X. MNMST: topology of cell networks leverages identification of spatial domains from spatial transcriptomics data. Genome Biol. 2024;25(1):133.

[55] Wang X, Allen WE, Wright MA, Sylwestrak EL, Samusik N, Vesuna S, et al. Three-dimensional intact-tissue sequencing of single-cell transcriptional states. Science. 2018;361:eaat5691.

[56] Zeng H, Huang J, Ren J, Wang CK, Tang Z, Zhou H, et al. Spatially resolved single-cell translatomics at molecular resolution. Science. 2023;380(6652):eadd3067.

[57] Wake H, Lee PR, Fields RD. Control of local protein synthesis and initial events in myelination by action potentials. Science. 2011;333(6049):1647–1651.

[58] Zhang D, Deng Y, Kukanja P, Agirre E, Bartosovic M, Dong M, et al. Spatial epigenome–transcriptome co-profiling of mammalian tissues. Nature. 2023;616(7955):113–122.

[59] Chen M, Wei Z, Huang Z, Ding B, Li Y. Simple and deep graph convolutional networks. In: International conference on machine learning. PMLR; 2020. p. 1725–1735.

[60] Zhang H, Wu Q, Yan J, Wipf D, Yu PS. From canonical correlation analysis to self-supervised graph neural networks. Advances in Neural Information Processing Systems. 2021;34:76–89.

[61] Li L, Li Z, Zakharchenko V, Chen J, Li H. Advanced 3D motion prediction for video-based dynamic point cloud compression. IEEE Transactions on Image Processing. 2019;29:289–302.

[62] Williams C, Seeger M. Using the Nyström method to speed up kernel machines. Advances in neural information processing systems. 2000;13.

[63] Xiao Z, Cui L, Yuan Y, He N, Xie X, Lin S, et al. 3D reconstruction of a gastrulating human embryo. Cell. 2024;187(11):2855–2874.

[64] Hu Y, Xie M, Li Y, Rao M, Shen W, Luo C, et al. Benchmarking clustering, alignment, and integration methods for spatial transcriptomics. Genome Biology. 2024;25(1):212.

[65] Wolf FA, Angerer P, Theis FJ. SCANPY: large-scale single-cell gene expression data analysis. Genome Biol. 2018;19:1–5.

[66] Wu T, Hu E, Xu S, Chen M, Guo P, Dai Z, et al. clusterProfiler 4.0: A universal enrichment tool for interpreting omics data. Innovation. 2021;2:100141.

[67] Palla G, Spitzer H, Klein M, Fischer D, Schaar AC, Kuemmerle LB, et al. Squidpy: a scalable framework for spatial omics analysis. Nat Methods. 2022;19:171–178.

[68] Yu W, Xiaoke M, Zaiyi L.: Network model for alignment, stitching and slice-to-volume 3D reconstruction of large-scale spatially resolved slices. Zenodo. https://doi.org/10.5281/zenodo.18815221 (2026).

Acknowledgements

We thank the members of the Ma Lab for helpful discussions, and appreciate the researchers who provided us with the source code for comparison. This work was supported by the Noncommunicable Chronic Diseases-National Science and Technology Major Project (Grant Nos. 2024ZD0531100 and 2024ZD0531103 to X.M), the Joint Funds of the National Natural Science Foundation of China (Grant No. U22A20345 to X.M), the Natural Science Basic Research Program of Shaanxi (Grant No. 2025JC-QYCX-057 to X.M), the Xidian University Specially Funded Project for Interdisciplinary Exploration (Grant No. TZJHF202507 to X.M), and the R&D-Oriented Science and Technology Program Projects of Guyuan City (Grant No. 2025GKJYF0002 to Y.W.).

Author Contributions

Z.L. and X.M. conceived and designed the study. X.M., Z. L. and Y.W. performed the research. Y.W. collected and constructed the benchmark datasets and models. Y.W., Z. L. and X.M. completed the downstream analysis.

Competing interests

The authors declare that they have no competing interests.

Figure Legends

Figure 1. Overview of GEASO. A. Key challenges for aligning, stitching and 3D reconstructing of spatially resolved slices, including rigid transformation (scale, rotation, and translation), non-rigid transformation (local deformation), partial overlapping, and large-scale dataset. **B.** GEASO consists of three modules, i.e., feature learning, elastic registration and acceleration strategies, where the first procedure learns consistent features of spots by integrating spatial and expression profile with graph learning, elastic registration addresses both rigid and non-rigid transformation of slices, and the acceleration module extends application of GEASO for large-scale slices with low-rank approximation of matrices, voxel-based down-sampling and Gaussian process interpolation. **C.** Typical applications of GEASO include pairwise alignment and stitching of partially overlapping slices (left), slice-to-volume 3D reconstruction and visualization of tissue architecture in 3D space (middle), and topology analysis in 3D space (right).

Figure 2. Performance of algorithms on the alignment, stitching, and slice-to-volume 3D reconstruction of spatial slices. A. Visualization of adjacent mouse brain slices with different rotation angles, and alignment results obtained by different algorithms with their PCC values, where spots in source slice are colored in orange, and in target are colored in blue. **B.** Radar charts of CLC (left) and AAS (right) of various algorithms for aligning mouse brain slices with different rotation angles. **C.** Visualization of stitching of slices generated by STARmap with different overlapping ratios and rotation angles, where spots in source slice are colored in orange, and in target are colored in blue. **D.** Barplot of MAE (mean absolute error) of various algorithms for stitching slices with under different rotation angles and overlap ratios. **E.** Visualization of slice-to-volume 3D reconstruction and barplot of MAE on mouse hemibrain slices sequenced using MERFISH. Data are presented as mean values, with error bars indicate the 95% confidence intervals. Individual data points are overlaid to show the data distribution ($n = 128$ biologically independent pairwise alignments, derived from 129 sequential spatial slices). **F.** Visualization of slice-to-volume 3D reconstruction and barplot of CLC on human lymph node slices sequenced using OpenST. Data are presented as mean values, with error bars indicate the 95% confidence intervals. Individual data points are overlaid to show the data distribution ($n = 18$ biologically independent pairwise alignments, derived from 19 sequential spatial slices). **G.** Memory usage of different algorithms for slice alignment by varying the number of cells. Source data are provided as a Source Data file.

Figure 3. Performance of GEASO for bridging different platforms with various resolutions and genome coverage. A. Illustration of zones of H&E image of breast cancer section covered by Xenium and Visium platforms. **B.** Visualization of spatial distribution of cell types for Xenium and Visium slices. **C.** Visualization of stitching results obtained by GEASO between two Xenium slices, where the region surrounded by solid squares corresponds to DCIS. **D.** Spatial distribution of DCIS in single Xenium slice and the stitched slice (top), and sub-networks of DCIS in each graph of cells in various slices. **E.** Distribution of cells inside and outside of DCIS in

terms of degree (top) and closeness (bottom). For all boxplots, the center line represents the median, box limits represent the upper and lower quartiles (25th and 75th percentiles), and the whiskers represent 1.5× the interquartile range. The sample sizes n represent individual cells ($n = 1,416$ for Sample 1, $n = 1,325$ for Sample 2, and $n = 1,565$ for the stitched sample). P values are calculated using the two-sided Mann-Whitney U test. **F.** Illustration of overlapped region between the stitched Xenium and Visium slice. **G.** Spatial distribution of cancer-marker gene *ABCC11* in the Visium (top) and stitched Xenium slice (bottom). **H.** Spatial distribution of different cell types in overlap region of Xenium slice (left), and the corresponding bio-marker genes in Visium slice (middle), and imputed bio-marker genes in Xenium slices (right). Source data are provided as a Source Data file.

Figure 4. GEASO tracks evolution of organs with slice-to-volume 3D reconstruction. A. Visualization of serial slices of mouse embryo (left) and the reconstructed 3D embryo by GEASO (right) at E9.5, where points correspond to spots are colored by annotated spatial domains. **B.** Visualization of serial slices of mouse embryo (left) and the reconstructed 3D embryo by GEASO (right) at E11.5. **C.** Visualization of the reconstructed 3D embryo by baselines, and boxplots of CLC scores obtained by different methods at E9.5 (left) and E11.5 (right). For all boxplots in **C**, **F**, and **G**, the center line represents the median, box limits represent the upper and lower quartiles (25th and 75th percentiles), and the whiskers represent 1.5× the interquartile range. The sample sizes n represent biologically independent pairwise alignments derived from sequential spatial slices ($n = 89$ pairs from 90 slices for E9.5, $n = 83$ pairs from 84 slices for E11.5). P values are calculated using two-sided Mann-Whitney U test. **D.** Visualization of 3D architecture of Heart and Liver (left), and spatial distribution of bio-marker genes *Myl7* and *Afp* at E9.5. **E.** Visualization of 3D architecture of Heart and Liver (left), and spatial distribution of bio-marker genes *Myl7* and *Afp* at E11.5. **F.** Visualization of topology of Heart and Liver, and boxplot showing the distribution of degrees of spots within the Heart and Liver at E9.5. The sample sizes n represent individual spots ($n = 49,461$ spots for Heart, $n = 2,623$ spots for Liver). P value is calculated using the two-sided Mann-Whitney U test ($P < 2.2 \times 10^{-226}$). **G.** Visualization of topology of Heart and Liver, and boxplot showing the distribution of degrees of spots within the Heart and Liver at E11.5. The sample sizes n represent individual spots ($n = 108,060$ spots for Heart, $n = 128,761$ spots for Liver). P value is calculated using the two-sided Mann-Whitney U test ($P < 2.2 \times 10^{-226}$). **H.** Generation of pseudo-slices at custom directions from reconstructed 3D architecture of mouse embryo. Source data are provided as a Source Data file.

Figure 5. GEASO enables biomarker discovery across distinct organs. A. Visualization of 3D architecture of mouse embryo reconstructed by GEASO, and the spatial distribution of major organs within the 3D context. **B.** The anatomical atlas of mouse brain (left) and the manually annotated 3D architecture of the brain (right). **C.** The dotplot of differentially gene expression analysis for sub-structure of mouse brain within 3D context. **D.** Spatial distribution of differentially expressed genes

(DEGs) across mouse brain sub-structures within 3D context. "Figure 5B" created in BioRender. Wang, Y. (https://BioRender.com/3f66vm3) is licensed under CC BY 4.0.

Figure 6. GEASO also applicable to alignment of cross-modality slices. A. Schematic workflow of GEASO for aligning two adjacent cross-modality STARmap (RNA) and RIBOmap (protein) slices sequenced from mouse brain, where cells are colored by annotated cell types. **B.** Spatial distribution of single-cell relative translation efficiency (scRTE) for cell-type-specific biomarkers in the RIBOmap slice. Cells of the annotated cell type with available scRTE values are colored by scRTE levels, while others are colored in gray, and the boxplots below compare the expression level of corresponding marker genes between the STARmap and RIBOmap slices. For allbox plots, the center line represents the median, box limits represent the upper and lower quartiles (25th and 75th percentiles), and the whiskers represent 1.5× the interquartile range. The sample sizes n represent individual cells ($n = 8,849$ STARmap cells and $n = 8,999$ RIBOmap cells for Oligodendrocytes, $n = 18,800$ STARmap cells, and $n = 17,827$ RIBOmap cells for Telencephalon interneurons). P values are calculated using the two-sided Mann-Whitney U test ($P < 2.2\times10^{-226}$ for *Fth1*, $P < 2.2\times10^{-226}$ for *Mbp*, $P = 6.5\times10^{-53}$ for *Qdpr*, $P = 3.0\times10^{-26}$ for *Eef1a1*, and $P < 2.2\times10^{-226}$ for *Kif5a*). **C.** Visualization of spatial position of RNA and *H3K4me3* sequenced regions within P22 juvenile mouse brain tissue. **D.** Visualization of spatial transcriptomics and *H3K4me3* slices, where spots are colored by annotated regions. **E.** The spatial distributions of two regions before and after slice alignment. **F.** Confusion matrix of region correspondences before and after slice alignment. Barplots on the axis represents the counts of all regions. Source data are provided as a Source Data file.

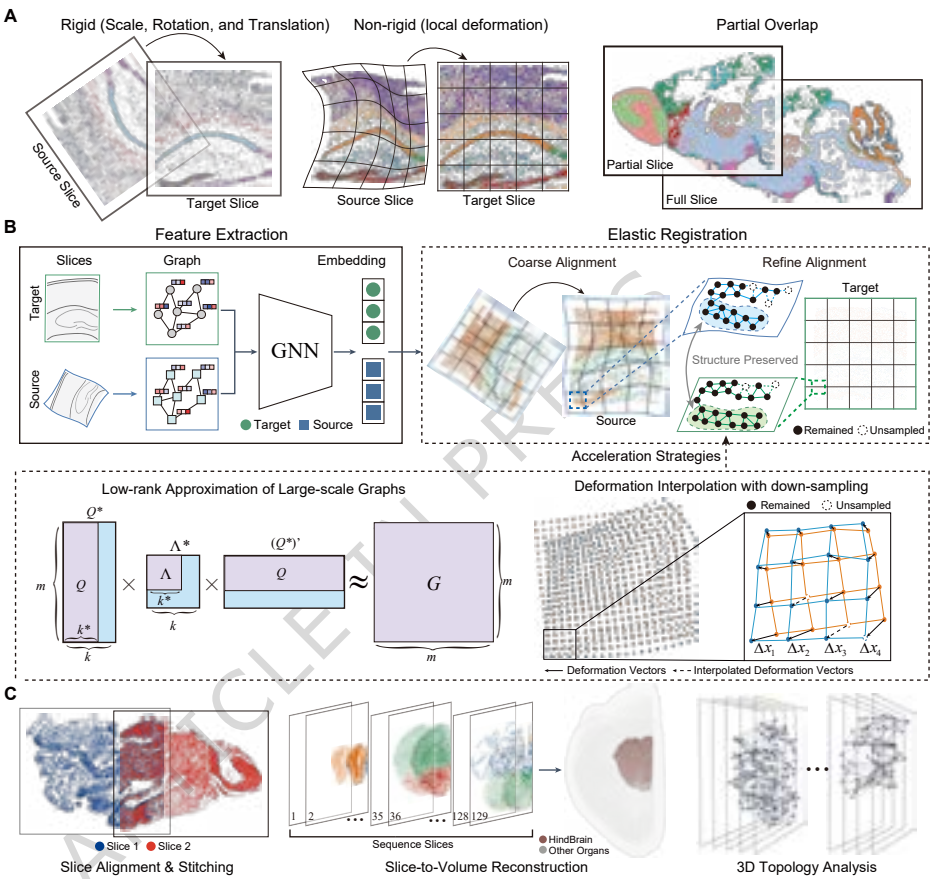
A
Rigid (Scale, Rotation, and Translation)
Non-rigid (local deformation)
Partial Overlap
Source Slice
Target Slice
Source Slice
Target Slice
Partial Slice
Full Slice
B
Feature Extraction
Slices
Graph
Embedding
Target
Source
GNN
Target
Source
Elastic Registration
Coarse Alignment
Refine Alignment
Target
Structure Preserved
Source
Remained
Unsampled
Acceleration Strategies
Low-rank Approximation of Large-scale Graphs
Deformation Interpolation with down-sampling
Remained
Unsampled
Deformation Vectors
Interpolated Deformation Vectors
C
Slice 1
Slice 2
Slice Alignment & Stitching
Sequence Slices
HindBrain
Other Organs
Slice-to-Volume Reconstruction
3D Topology Analysis

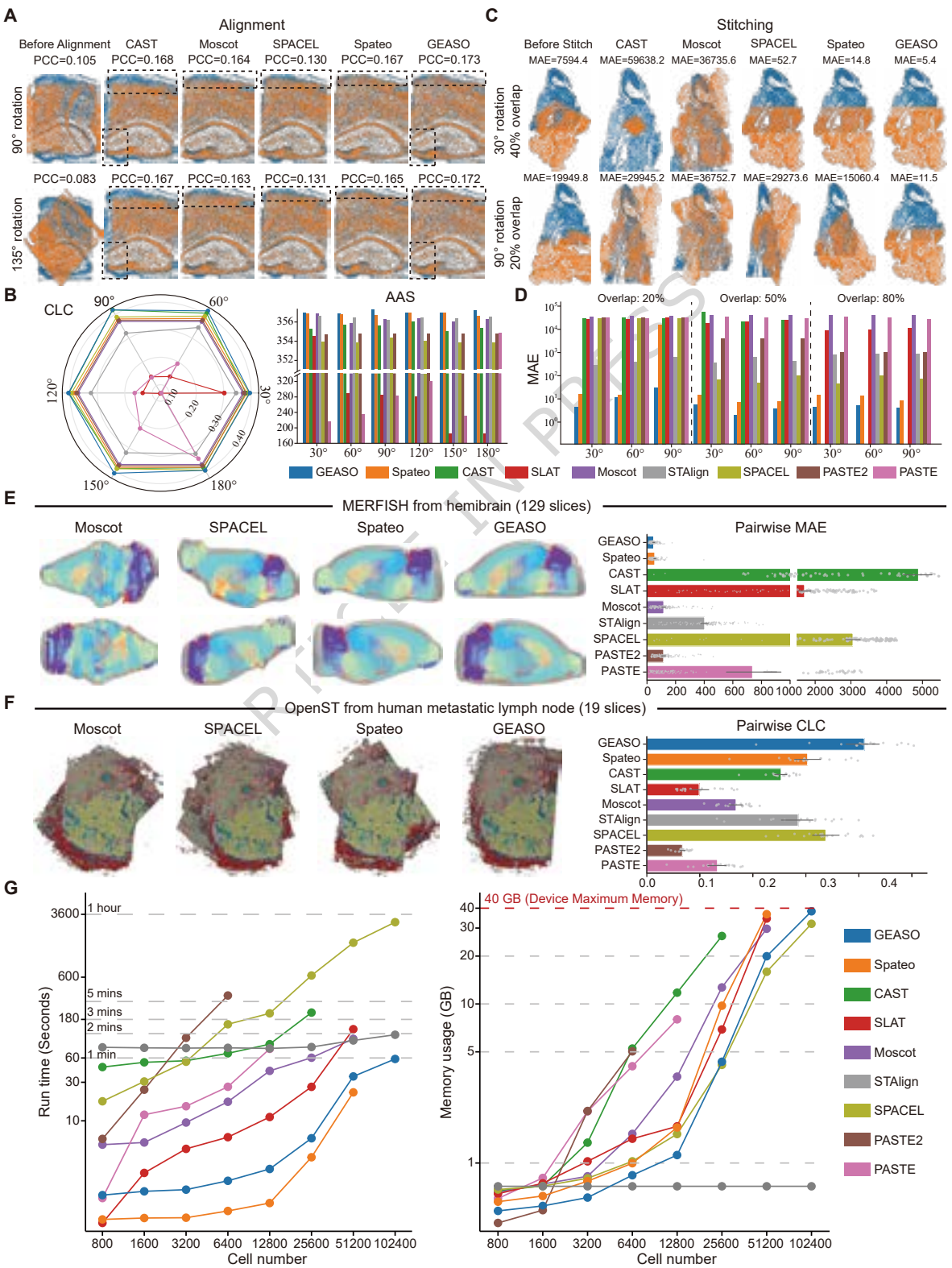

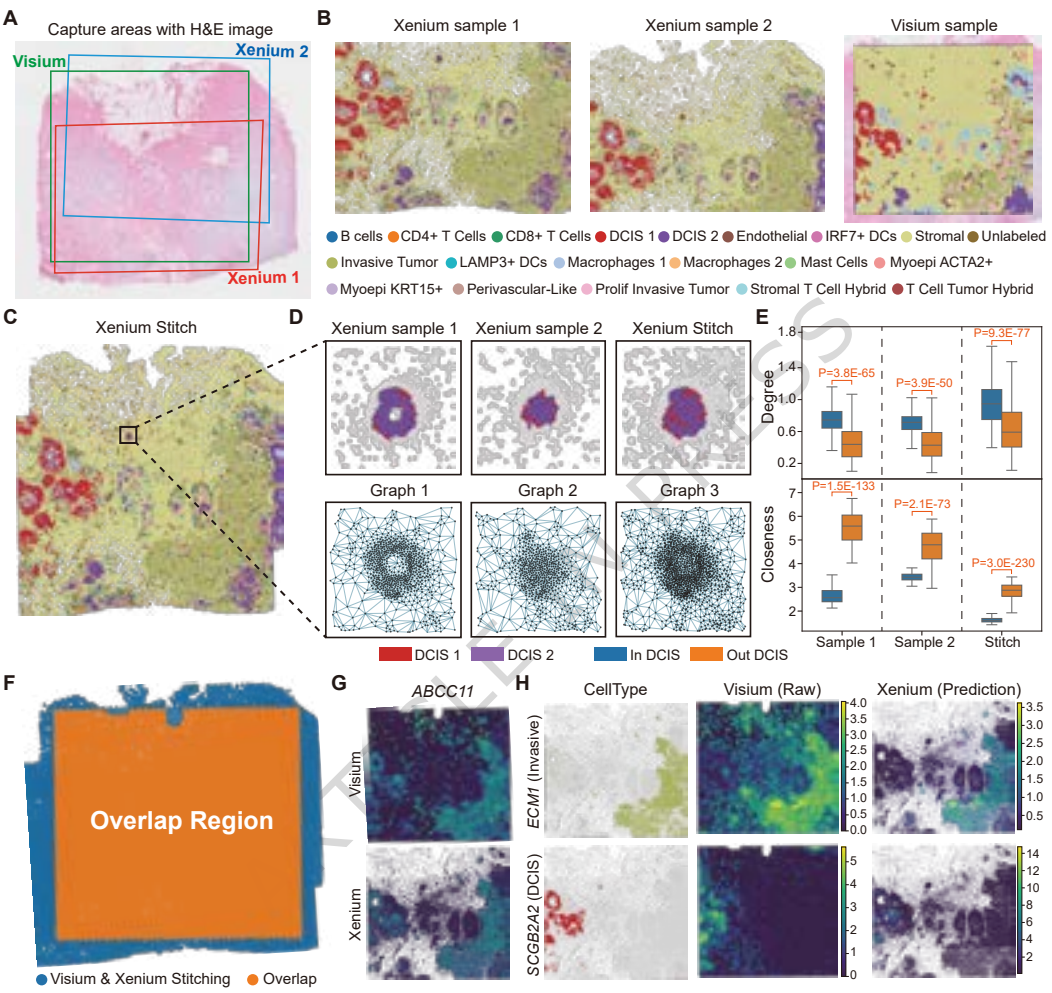
A
Capture areas with H&E image
Visium
Xenium 2
Xenium 1
B
Xenium sample 1
Xenium sample 2
Visium sample
B cells
CD4+ T Cells
CD8+ T Cells
DCIS 1
DCIS 2
Endothelial
IRF7+ DCs
Stromal
Unlabeled
Invasive Tumor
LAMP3+ DCs
Macrophages 1
Macrophages 2
Mast Cells
Myoepi ACTA2+
Myoepi KRT15+
Perivascular-Like
Prolif Invasive Tumor
Stromal T Cell Hybrid
T Cell Tumor Hybrid
C
Xenium Stitch
D
Xenium sample 1
Xenium sample 2
Xenium Stitch
Graph 1
Graph 2
Graph 3
DCIS 1
DCIS 2
In DCIS
Out DCIS
E
Degree
P=3.8E-65
P=3.9E-50
P=9.3E-77
Closeness
P=1.5E-133
P=2.1E-73
P=3.0E-230
Sample 1
Sample 2
Stitch
F
Overlap Region
Visium & Xenium Stitching
Overlap
G
ABCC11
Visium
Xenium
H
CellType
Visium (Raw)
Xenium (Prediction)
ECM1 (Invasive)
SCGB2A2 (DCIS)

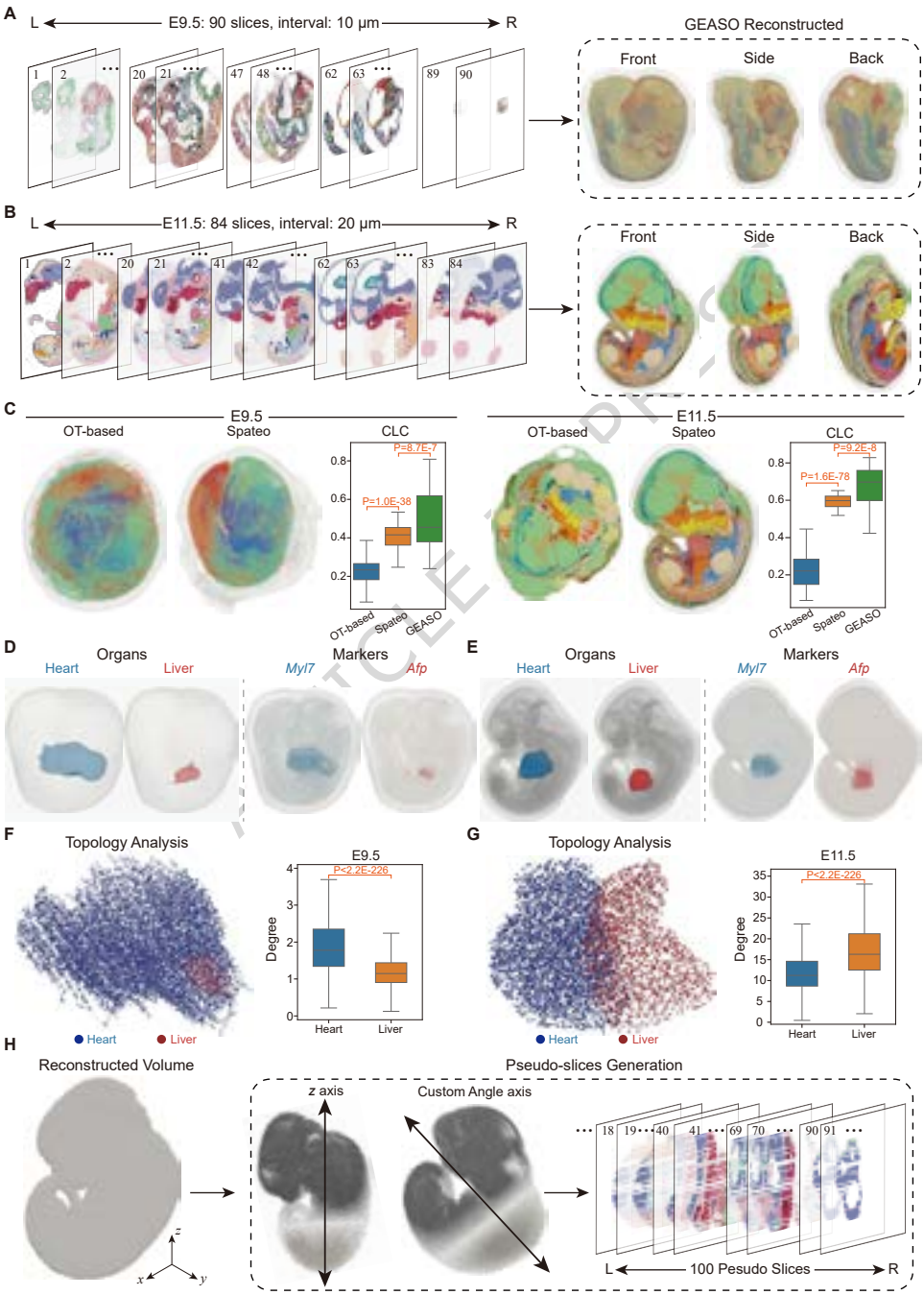
A
L
E9.5: 90 slices, interval: 10 μm
R
GEASO Reconstructed
Front
Side
Back
B
L
E11.5: 84 slices, interval: 20 μm
R
Front
Side
Back
C
E9.5
OT-based
Spateo
CLC
P=8.7E-7
P=1.0E-38
OT-based
Spateo
GEASO
E11.5
OT-based
Spateo
CLC
P=9.2E-8
P=1.6E-78
OT-based
Spateo
GEASO
D
Organs
Heart
Liver
Markers
Myl7
Afp
E
Organs
Heart
Liver
Markers
Myl7
Afp
F
Topology Analysis
E9.5
P<2.2E-226
Degree
Heart
Liver
Heart
Liver
G
Topology Analysis
E11.5
P<2.2E-226
Degree
Heart
Liver
Heart
Liver
H
Reconstructed Volume
z
x
y
Pseudo-slices Generation
z axis
Custom Angle axis
L
100 Pesudo Slices
R

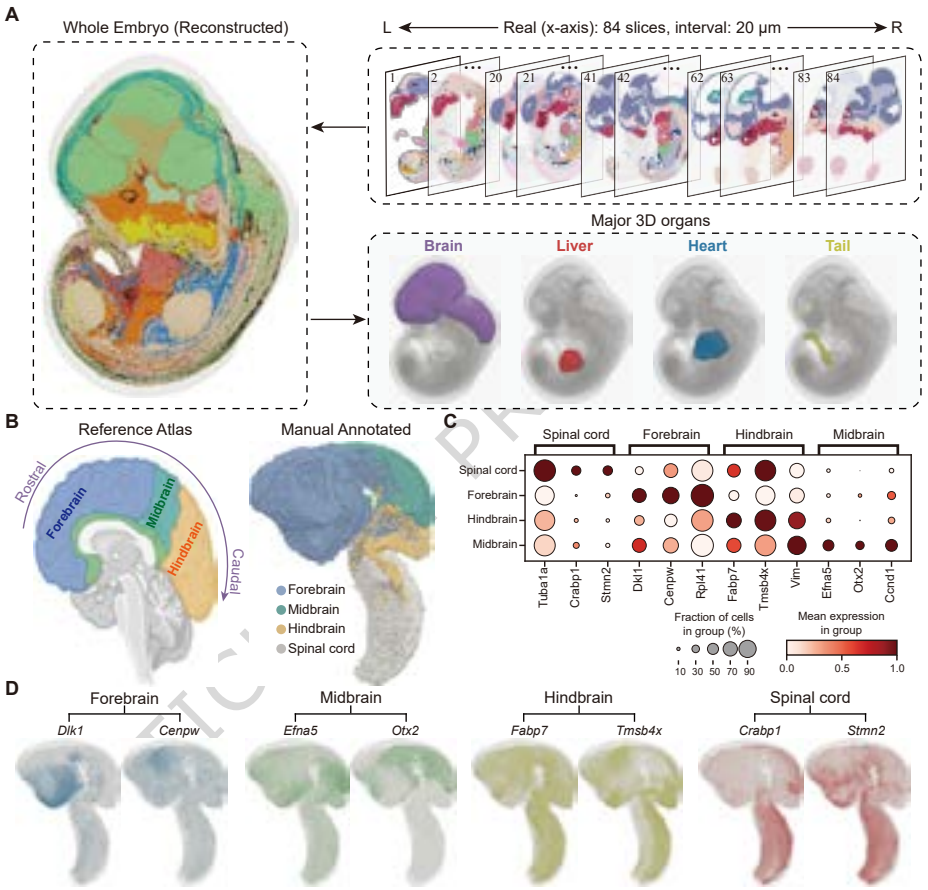
A
Whole Embryo (Reconstructed)
L
Real (x-axis): 84 slices, interval: 20 μm
R
1
2
20
21
41
42
62
63
83
84
Major 3D organs
Brain
Liver
Heart
Tail
B
Reference Atlas
Manual Annotated
Rostral
Caudal
Forebrain
Midbrain
Hindbrain
Spinal cord
C
Spinal cord
Forebrain
Hindbrain
Midbrain
Tuba1a
Crabp1
Stmn2
Dkl1
Cenpw
Rpl41
Fabp7
Tmsb4x
Vim
Efna5
Otx2
Ccnd1
Fraction of cells in group (%)
10 30 50 70 90
Mean expression in group
0.0 0.5 1.0
D
Forebrain
Dlk1
Cenpw
Midbrain
Efna5
Otx2
Hindbrain
Fabp7
Tmsb4x
Spinal cord
Crabp1
Stmn2

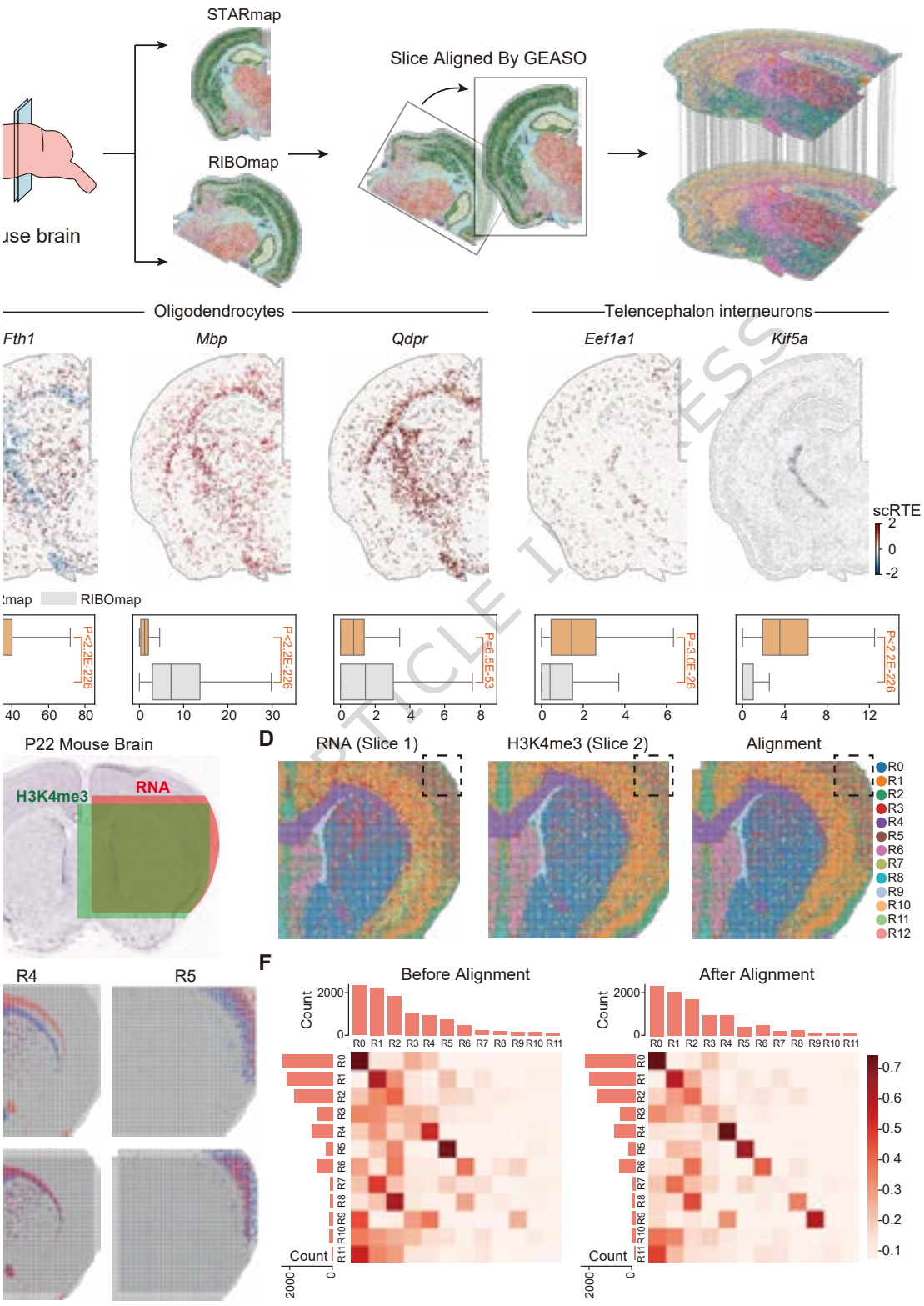
STARmap
RIBOmap
Slice Aligned By GEASO
use brain
Oligodendrocytes
Telencephalon interneurons
Fth1
Mbp
Qdpr
Eef1a1
Kif5a
scRTE
2
0
-2
RIBOmap
P<2.2E-226
P<2.2E-226
P=6.5E-53
P=3.0E-26
P<2.2E-226
40 60 80
0 10 20 30
0 2 4 6 8
0 2 4 6
0 4 8 12
P22 Mouse Brain
H3K4me3
RNA
D
RNA (Slice 1)
H3K4me3 (Slice 2)
Alignment
R0
R1
R2
R3
R4
R5
R6
R7
R8
R9
R10
R11
R12
R4
R5
F
Before Alignment
After Alignment
Count
2000
0
R0 R1 R2 R3 R4 R5 R6 R7 R8 R9 R10 R11
0.7
0.6
0.5
0.4
0.3
0.2
0.1